ORIGINAL ARTICLE

Automated bone contour detection in ultrasound B-mode images for minimally invasive registration in computer-assisted surgery – an *in vitro* evaluation

Jens Kowal[1]*
Christoph Amstutz[2]
Frank Langlotz[1]
Haydar Talib[1]
Miguel Gonzalez Ballester[1]

[1]*MEM Research Centre for Orthopaedic Surgery, at the University of Bern, Stauffacherstrasse 78, CH-3014 Bern, Switzerland*

[2]*University Hospital Zürich, Raemistrasse 100, CH-8091 Zürich, Switzerland*

Correspondence to: Jens Kowal, MEM Research Centre for Orthopaedic Surgery, at the University of Bern, Stauffacherstrasse 78, CH-3014 Bern, Switzerland. E-mail: jk@memcentre.unibe.ch

Abstract

Background   Minimally invasive surgical interventions performed using computer-assisted surgery (CAS) systems require reliable registration methods for pre-operatively acquired patient anatomy representations that are compatible with the minimally invasive paradigm. The use of brightness-mode ultrasound seems to be promising, if associated devices work in a computationally efficient and fully automatic manner.

Methods   This paper presents a rapid and fully automatic segmentation approach for ultrasound B-mode images capable of detecting echoes from bony structures. The algorithm focuses on the precise and rapid detection of bone contours usable for minimally invasive registration. The article introduces the image-processing scheme and a set-up enabling a direct comparison between manually digitized reference points and the segmented bone contours. The segmentation accuracy was assessed using cadaveric material.

Results   The experimental evaluation revealed results in the same order of magnitude as a pointer-based surface digitization procedure.

Conclusion   The suggested segmentation approach provides a reliable means of detecting bony surface patches in ultrasound images. Copyright © 2007 John Wiley & Sons, Ltd.

Keywords   ultrasound; automatic bone contour segmentation; registration

Introduction

Surgical interventions guided by passive navigation systems are well established in the orthopaedic area   (1). Precise registration is vital for surgical navigation systems that utilize pre-operatively acquired anatomical representations, such as computed tomography (CT) datasets. The purpose of the registration procedure is to provide a transformation for the representation of the anatomy in the coordinate system that is defined by an intra-operatively attached reference base (2). The current registration techniques deliver reliable registration accuracy, but only if the anatomical structures are exposed and accessible to the surgeon (3).

In recent years, minimally invasive surgical techniques have become more relevant in computer-assisted orthopaedic interventions. In order to register representations of patient anatomy, reliable procedures that are in compliance with the minimally invasive paradigm are required. It has been shown that both ultrasound amplitude-mode (A-mode) and brightness-mode (B-mode) devices can be used as a tool for minimally invasive registration (4–9).

Tonetti *et al*. (9) used manually digitized bone contour points from B-mode ultrasound images for the registration of a pelvis with appropriate accuracy. However, the clinical acceptance of such a B-mode ultrasound registration method can only be achieved when the surgeon's interaction with the system is minimized via automation of the contour segmentation process (1).

Several groups have proposed solutions for automatic ultrasound image segmentation, specifically with the extraction of bone contours (4,5,7,10). Amin *et al*. (4) proposed the use of an initial registration in conjunction with the CT dataset to deliver an initial estimation of the image area that contains the bony surface. An edge detector was then utilized to extract the actual bone contour. Ionescu *et al*. (7) suggested a segmentation approach intended for use with automatic soft tissue registration. This approach uses the watershed segmentation method, and it was reported that the system was also capable of segmenting pelvic surfaces automatically. Thomas *et al*. (10) proposed an automatic segmentation approach, mainly based on morphological operations, to estimate the femur length in fetal ultrasound images. The reported results indicate a good agreement between the automatically calculated and the manually determined length of the femur. The time required to perform the processing of a single image (10 min) would not be acceptable for an intra-operative registration process. However, with the performance improvements of today's computer hardware, shorter execution times than the published ones are very likely. Roche *et al*. (11) published a method to register pre-operative magnet resonance images with intra-operatively acquired three-dimensional (3D) ultrasound images by using maximization of the similarity measure, which does not require an explicit segmentation step for the 3D ultrasound images. The use of fuzzy logic in combination with *a priori* knowledge about the osseous interface and ultrasound imaging physics to segment automatically ultrasound images has been suggested by Daanen *et al*. (12). By using spatially separated ultrasound images, Jain *et al*. (13) have investigated the exact location of the osseous interface in relation to the created echo. They further propose an automatic bone surface detection method, using a Bayesian probabilistic framework. Yu *et al*. (14) have examined the detection and localization performance of a squared version of the instantaneous coefficient of variation edge detector, and reported an improved performance compared to other detection algorithms, especially in the presence of noise. Unscented Kalman filters have been used by Moghari *et al*. (15)

to incrementally register bone surfaces extracted from 3D ultrasound images with surfaces originated from CT datasets. Recently, Barratt *et al*. (6) published a promising method, which tries to combine the necessary ultrasound probe calibration step with the actual registration in a single automatic procedure.

In this article, a fully automatic segmentation approach is presented to identify bone contours in B-mode ultrasound images. An experimental set-up is described that enables the computation of the lower bound of the segmentation accuracy. Furthermore, the results of an extensive cadaver study are presented, suggesting that the proposed algorithm delivers reliable information for percutaneous registration. In order to finally compute the actual registration, the segmented bone contours are sub-sampled into discrete points and these points are then used to compute the registration matrix, with the help of the algorithm suggested by Bächler *et al*. (16).

The proposed algorithm has meanwhile been used in an *in vivo* study during navigated spinal interventions. The results of that study will be presented in a future publication.

Materials and methods

The following subsections explain the fundamental ideas of the different filtering steps and their influence on the ultrasound images. An overview of the image-processing pipeline is given in Figure 1. A typical ultrasound image acquired during the experimental work is used to illustrate the effect of the different filtering steps (Figure 2a–h).
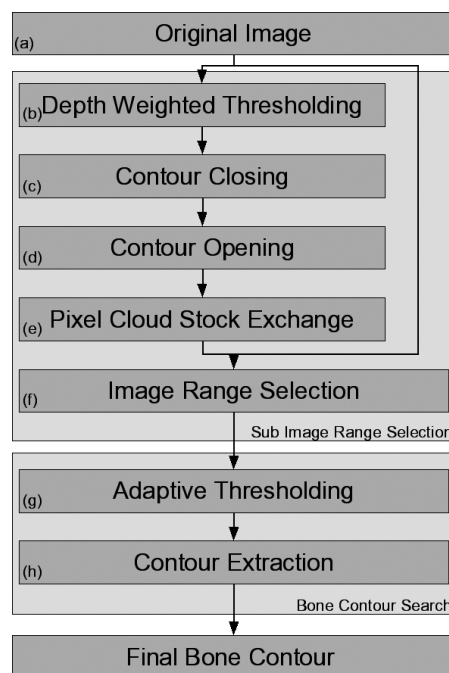
Figure 1. **Structural overview of the proposed image-processing pipeline. The processing is divided into two main parts, the sub-image range selection step, and the bone contour search step. Panels (a)–(h) correspond to the panels in Figure 2**

Summary of the image-processing approach

Since the proposed segmentation method should be applicable to a large set of anatomical regions, no *a priori* information about the anatomy to segment has been included. The other main criteria guiding the development of the segmentation method were segmentation accuracy, computational efficiency and the demand for a fully automatic segmentation. Ultrasound images are created by the reflection of the ultrasound waves at tissue interfaces. The reflection intensity corresponds to the reflection coefficient *R*, which can be calculated from the two acoustic impedances, Z' and Z'' $\left(R = \left(\frac{Z'' - Z'}{Z'' + Z'} \right)^2 \right)$. Strong reflection occurs if the ultrasound waves traverse from a medium with small acoustic impedance (Z') to a medium behind the interface with high acoustic impedance (Z''). The interface between soft tissue and bone matches these conditions. Almost all of the traversing ultrasound waves are reflected from the bony surface. This results in a strong reflection from the soft tissue–bone interface, with concomitant high image contrast in that area. The suggested approach uses this effect and identifies the deepest connected bright structure shown in the image.

The segmentation process is subdivided into two main steps. In the first step, referred to as the *sub-image range selection* step, the algorithm identifies the region that most likely contains the bone contour in the original image. Then within this region, the second step, the *bone contour search* step, extracts the actual bone contour.

Sub-image range selection

As a first step, a depth-weighted threshold is applied to the original image. The image pixel value is thereby adjusted based on its position in the image. This compensates for the higher attenuation rates that affect echoes generated from deeper structures. The adjusted pixel value $\hat{p}_{[x,y]}$ is computed as the product of the original pixel value $p_{[x,y]}$ and its row position $y^{w_{TRow}}$ (equation 1), where w_{TRow} is an empirically determined weight controlling the influence of the depth. Of the resulting pixel column sets $\hat{P}_x$ (equation 2), the n_{TPix} brightest pixels are taken within each column *x* according to equation 3. As output, a binary image (equation 4) containing a limited number of pixels per column is generated (Figure 2b):

$$\hat{p}_{[x,y]} = p_{[x,y]} \cdot y^{w_{TRow}} \tag{1}$$

$$\hat{P}_x : \{\hat{p}_{[i,j]} | i = x, 0 \leq j \leq y_{\max}\} \tag{2}$$

$$\tilde{P}_x : \left\{ \tilde{p}_0 \ldots \tilde{p}_{n_{TPix}} \in \hat{P}_x \left| \begin{array}{cc} \forall & \forall \\ \tilde{p}_i \, \hat{p}_j \in \hat{P} \setminus \{\tilde{p}_0 \ldots \tilde{p}_{nTPix}\} \end{array} \tilde{p}_i \geq \hat{p}_j \right. \right\} \tag{3}$$

$$I_{Tresh} : \{\tilde{P}_i | 0 \leq i \leq x_{\max}\} \tag{4}$$

The next two filters utilize morphological image processing (17,18) to remove small groups of pixels as well as to fuse bigger groups of pixels in the processed binary image. First, a *closing operation* is applied to the image. This operation basically fills small and thin holes and connects nearby objects (Figure 2c). Then, the following *opening operation* removes remaining small and thin objects from the image (Figure 2d). In general, both operators smooth object boundaries in the image. Each morphological filter step uses a four-connected structuring element with a size of pixel 3×3.

At this stage, the binary image consists of a diminished set of partially connected groups of pixels, referred to as 'pixel clouds'. The pixel clouds are defined as eight-connected components. Most of the speckle artifacts present in Figure 2b have been removed by the morphological filter combination. Some of the remaining pixel clouds represent single echoes originating from the same anatomical structure. The inherent connectivity has been lost, either by disturbances during the actual image creation process in the ultrasound device or by the applied processing steps. The final step in the *sub-image range selection process* tries to spot and restore some of these potential connections between adjacent pixel clouds. An iterative extension to a connected component labelling approach (19) is used, referred to by the authors as *pixel cloud stock exchange*.

Prior to the iteration process, all identified pixel clouds are assigned a value that represents their initial *trading value*. These values are determined based on both pixel properties and topological cloud properties. The value V_A of a cloud *A* is calculated as the weighted sum, according to equation 5; $V_{A,Pix}$ is the sum over all grey-values of the group members in the original image (equation 6); $|X_A|$ represents the spreading of *A* over the columns of the image (equation 7); $|Y_A|$ represents the spreading of *A* over the rows of the image (equation 8); and $V_{A,Pos}$ corresponds to the centred position of cloud *A* with respect to the upper edge of the image (equation 9):

$$V_A = V_{A,Pix} + w_{Col} \cdot |X_A| + w_{Row} \cdot |Y_A| + w_{Pos} \cdot V_{A,Pos} \tag{5}$$

$$V_{A,Pix} = \sum_{[x,y] \in A} p_{[x,y]} \tag{6}$$

$$X_A : \{x | \exists y : [x,y] \in A\} \tag{7}$$

$$Y_A : \{y | \exists x : [x,y] \in A\} \tag{8}$$

$$V_{A,Pos} = \frac{\sum\limits^{Y_A} y_i}{|Y_A|} \tag{9}$$

The value for a cloud that spreads over several columns is higher than that for a cloud that spreads over several rows. Furthermore, clouds with the same shape have lower associated values, the closer they are to the upper edge of the image, i.e. the closer they are to the ultrasound transducer surface. This scheme aims at assigning higher values to echoes from potentially deeper structures with flat shapes – a pattern often characteristic of bony surfaces. After this initialization, an iterative and selective accumulation process is started, in which every

pixel cloud tries to increase its own value by *buying* other clouds. Constraints are defined to control the actual iteration. If a cloud A wants to *buy* a cloud B, the current value V_A has to be bigger than V_B. The value ΔV_A added to cloud A (its accretion) will be computed as the difference of V_B and the spatial distance between the centres of A and B (equation 10):

$$\Delta V_A = V_B - \left| \overline{A_{center} B_{center}} \right| \qquad (10)$$

The rules defined above ensure that pixel clouds first *buy* clouds locally in their vicinity. As soon as clouds have increased their own value, they then extend their *buying* activities to more distant clouds. The iterative process leads to a continuously growing system of independent pixel clouds distributed over the image plane. It is time efficient and adequate to select just a certain percentage of the most valuable pixel clouds as potential consumers during the iteration process. The whole process stops if a particular cloud has accumulated a value that is v% (Table 1) above the values of all other clouds.

Figure 2e depicts the result of the range selection step. The figure shows in grey all members of the largest cloud and a black line that indicates the connection between the individual originating clouds. These locations are then used to select a sub-image out of the original image (Figure 2f). The sub-image is selected as a collar around the connection line of the largest cloud. The width ($cwidth$) of this collar is defined depending on the anatomical regions. Figure 2f shows the selected pixels from the original image and the black connection line

Table 1. Empirically determined parameter values of our scheme. These values were also used during the experimental evaluation of the segmentation algorithm

Filter	Parameter	Value
Depth rel. threshold	w_{TRow}	2.0
	n_{TPix}	5 pixel
Contour closing opening	shape	Four-connected
	size	3×3
Pixel cloud stock exchange	w_{Col}	2.0
	w_{Row}	1.0
	w_{Pos}	2.0
	v	200%
Image range selection	$cwidth$	20 pixel
Adaptive threshold	p	80%
	q	80%

from the previous filter step. The bone contour search step described in the next subsection is then applied to the selected sub-image only.

Bone contour search

As an initial step, we apply the same depth-weighted intensity transform that was used in step one of the *sub-image range selection*. The actual search for the bone surface contour is based on adaptive thresholding. It uses a grey-level histogram computed from the sub-image. From the histogram, the p% brightest pixels are selected. From the sub-image, q% of the deepest pixels (deeper pixels are the ones which are more distant from the transducer surface) per column are selected. Subsequently, the
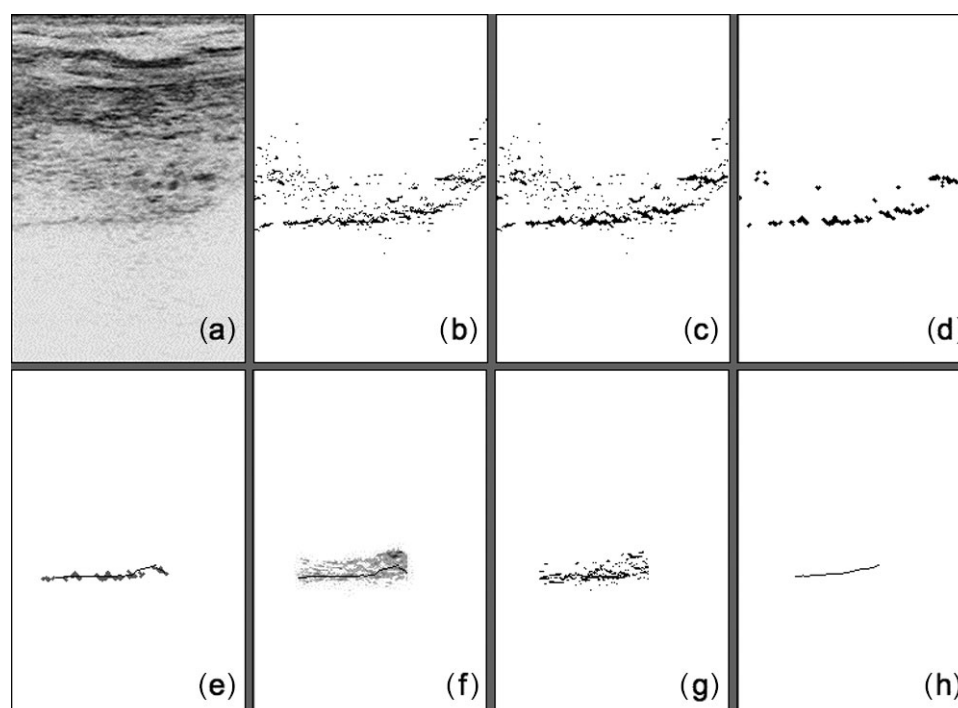
Figure 2. Output of the different image-processing steps, using a typical ultrasound image from a human pelvis; all images were inverted to improve visibility. (a) Original image; (b) depth-weighted thresholding filter; (c) contour closing filter; (d) contour opening filter; (e) pixel cloud stock exchange filter; (f) image range selection filter (including black connection line by pixel cloud stock exchange filter); (g) adaptive thresholding filter; (h) contour extraction filter

intersection set is computed between these two pixel sets. Figure 2g illustrates the results from this intersection. The actual values for p and q were determined during the evaluation and were stable across anatomical regions. A contour connecting the centres of each selected pixel column is then extracted from the thresholded image. As a final step, this contour is smoothed with a Gaussian kernel (Figure 2h).

Experimental set-up

As previously stated, the main issue addressed in this study was the computation of the practically achievable segmentation accuracy of the proposed segmentation approach, using fresh animal cadaver specimens. For this purpose, the spatial position of the segmented bone contours were compared with the results of a manual digitization of the same contours after resection of the soft tissue. An optical navigation system was used to track the positions and orientations of the instruments involved. The actual procedure is described in the following section.

A custom surgical navigation module implemented by the help of the open source framework MARVIN (20), running on a LINUX PC in conjunction with an optical navigation system (OPTOTRAK 3020, Northern Digital, Waterloo, Canada), was used to track the spatial positions of rigid bodies, such as the specimens, the ultrasound transducer and an additional reference pointer. According to its specification, the navigation system is able to track a single infrared light emitting diode with an accuracy of 0.1 mm. A conventional B-mode ultrasound device (Siemens Sonoline Sienna, Siemens AG, Erlangen, Germany) combined with a 7.5 MHz linear transducer was used to acquire the images. To determine the spatial orientation of the virtual image plane with respect to the coordinate system defined by the attached marker shield, the ultrasound transducer was calibrated according to the method presented in (21).

The images were acquired by using an eight-bit frame grabber board (WinTV, Hauppauge Computer Works, Hauppauge NY, USA) in standard S-VHS resolution. The part of the S-VHS video frame that contained the ultrasound image was defined during the calibration process (190×400 pixels; pixel resolution, $0.176 \text{ mm}^2/\text{pixel}$).

Fresh cadaveric specimens of bovine and porcine legs were used for the experiment. A dynamic reference base (DRB) was rigidly attached to track the movement of the specimens. All calculations were performed in the coordinate system defined by the attached DRB. As a first step, several sets of images from different anatomical regions of the specimens, together with their spatial positions, were acquired. In was ensured that all acquired images contained an echo that represented the actual bone contour line. Image quality-related parameters were adjusted at the ultrasound device to guarantee optimal conditions. Figure 3 shows a bovine specimen together with the navigated ultrasound transducer. The image acquisition process was performed in a temperature-controlled water bath to replicate the temperature conditions used during the probe calibration.

The segmentation was conducted for each acquired image. These results where then used to calculate 3D contour lines, based on the navigated transducer positions, i.e. the virtual image plane positions in the DRB coordinate system. The contour lines represent the bone surface at the positions where the inherent image penetrated the bone.

After all images were acquired and processed, the soft tissue surrounding the bone was removed to expose the bony surface. A tracked pointer was used to digitize reference contour points along the segmented contour lines. Figure 4 illustrates this digitization process. During the digitization, the pointer was aligned to coincide with the image plane, using the navigation system and the respective spatial position of the image. This specific, navigated pointer alignment aimed at digitizing the bone contour as closely as possible to the bone contour penetrating the image plane. Every misalignment of the pointer out of the image plane would most likely lead to an overestimation of the distance between the digitized contour and the automatically segmented bone contour. The reference contour points were digitized in such a way as to cover most of the segmented contour line for every image. The distance between adjacent digitized reference points in the image plane was <2 mm to ensure a rather dense point sequence per segmented ultrasound image.

Based on the specification of the navigation system and the geometry of the pointer used, the accuracy of the reference points digitized by the pointer was estimated to be <0.5 mm (22).

These reference points were chosen to be the *bronze standard* (23). For each reference point, the minimal distance to the respective segmented contour was computed. The average distance over all reference points represents the practically achievable segmentation accuracy.

Subsequently, an ANOVA test (24) was used to analyse whether the automatically segmented bone contours
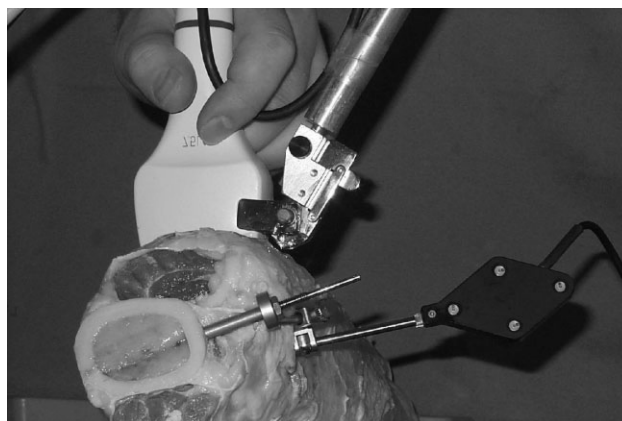
Figure 3. Image acquisition of a cadaveric bovine specimen. The anatomy and the ultrasound probe were tracked by the attached marker shields via the optical navigation system
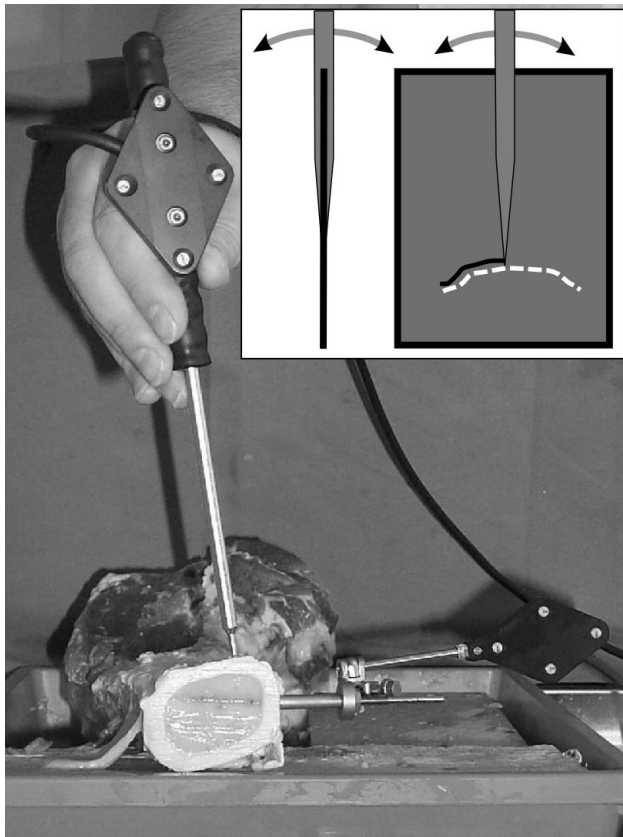
Figure 4. Manual digitization procedure for the reference contour points. The soft tissue has been removed from the specimen. With the help of the navigation system, the pointer was aligned with the previously stored image plane position. The reference points were used to compute segmentation accuracy

Table 2. Average error μ_{Error}, standard deviation σ_{Error}, and maximum error $\max_{Error}$ gained during the experimental study. Additionally, the average soft tissue depth $\mu_{STDepth}$ at the position where the image set was acquired is shown. The data are sorted both according to the examined specimens (rows B1–P5) and separated by anatomical region (diaphysial sets and distal sets). All values listed are in mm

Specimens		μ_{Error}	σ_{Error}	$\max_{Error}$	$\mu_{STDepth}$
Bovine	B1	0.58	0.29	0.77	63
	B2	0.47	0.14	0.73	61
Porcine	P1	0.33	0.15	0.68	39
	P2	0.35	0.21	0.64	43
	P3	0.42	0.19	0.91	34
	P4	0.41	0.22	0.67	35
	P5	0.38	0.13	0.59	45
Diaphysial sets	–	0.44	0.20	0.91	49
Distal sets	–	0.40	0.18	0.82	42
All specimens	–	0.42	0.19	0.91	46

are significantly different from the manually digitized reference contours.

For the experimental evaluation, seven intact animal leg specimens (five porcine and two bovine tibiae) were used. From every specimen, three image sets (each set included 10 images) were acquired, two from the diaphysial part and one from the distal part. Each image set contained 10 images. This led to a total of 210 images with their respective segmented bone contours and the corresponding reference point set created with the help of the navigated pointer. On average, a reference point set along each segmented contour line contained 12 points.

Results

All bone contours were segmented successfully. The segmentation process took 0.8 s on average. The iterative process of the pixel cloud stock exchange filter finished within three iterations in 90% of cases (with a maximum of six iterations overall). The parameters of our scheme were constant for the experiments at the values displayed in Table 1. The thickness of the soft tissue that was traversed by the ultrasound waves varied from 30 to 80 mm. The distance calculation for the automatically segmented contour lines and the reference contour points

resulted in an overall average error of 0.42 mm and a standard deviation (SD) of 0.19 mm. The average error μ_{Error}, SE σ_{Error} and maximum error $\max_{Error}$, separated both by the specimens and the anatomical regions, are summarized in Table 2. Additionally, Table 2 includes the average soft tissue depths $\mu_{STDepth}$ that were measured during the soft tissue removal at the positions where the image sets were acquired. Figure 5 illustrates a typical image distribution from a single anatomical region of a bovine leg specimen. The image frames are displayed with their corresponding segmented bone contour lines. Additionally, one ultrasound image is shown to illustrate the location of the images.

The ANOVA test performed was unable to reveal statistically relevant differences between the automatically segmented bone contours and the manually digitized reference contour points.
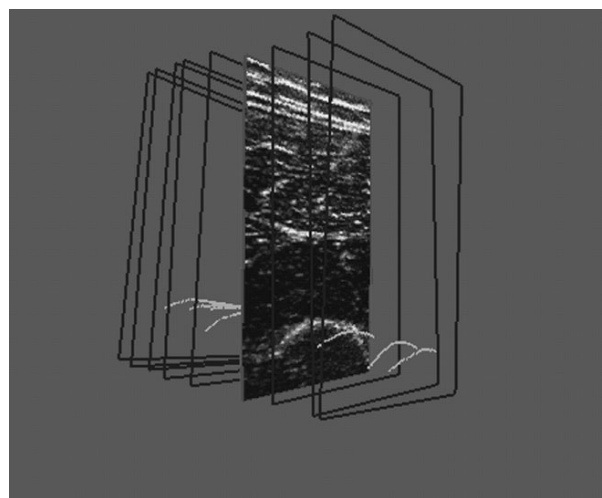

Figure 5. A typical set of ultrasound images from a cadaveric bovine specimen acquired in our experiments. All image frames are shown, together with their corresponding segmented bone contours. One selected ultrasound image of the image set is also shown

Discussion

Our multistage segmentation process was completed successfully without requiring any manual intervention. The algorithmic approach to divide the image processing into two main parts, first a preprocessing step that restricts the image area to a sub-image, and second the actual bone contour search in the restricted sub-image, was shown to provide a rapid, stable and accurate segmentation in our experiments. Additionally, the approach enables the future use of more computationally expensive image-processing steps for the actual contour search while retaining a rapid execution speed.

The segmentation accuracy depends on the quality of the images that are provided. From the working principle of the algorithm, it can be concluded that the segmentation will deliver more reliable results the better the contrast conditions are, especially in deeper soft tissue structures. This has not been evaluated in the course of the present study. However, it is of advantage to have a skilled sonographer to acquire the images during the clinical evaluation. In addition, an inherent mechanism to score the ultrasound images for removing those with lower quality could improve the reliability of the system.

The use of cadaveric specimens in a controlled laboratory environment provided appropriate conditions to investigate the practically achievable segmentation accuracy. The experimental approach to manually digitize the real bone surface that penetrates the virtual image plane provides the best estimation of the real surface that could be obtained in a clinical set-up, and it is therefore considered to be the 'bronze standard' for this study.

The experimental results show that the automatic image segmentation can deliver results whose accuracy is of the same order of magnitude as that of manual pointer digitization. Furthermore, the fact that all the tests were performed at distinctively different anatomical areas of several specimens of the two different species indicates that the segmentation could deliver reliable results over a wide range of soft tissue thicknesses.

One limitation of this study is the absence of an inter-observer analysis. Repeated measurements are difficult to conduct because of the irreversibility of the necessary soft-tissue resection prior to the manual digitization step of the reference contour points. However, the acquisition of multiple images within one image set was an attempt to compensate for this.

Conclusion

In this study an automatic bone contour segmentation algorithm for ultrasound B-mode images has been proposed. The algorithm tries to identify the single, deepest contour that represents a part of the bony surface. These contours are intended to be used as surface points for a minimally invasive registration of bony structures. Therefore, the accuracy and speed of the algorithm are more essential than the completeness of the detected bone contour line with respect to the original ultrasound image. The proposed algorithm provides a solution to this specific image segmentation problem. Moreover, the computed results provide support that our algorithm delivers results sufficiently accurate for minimally invasive registration of rigid anatomies during computer-assisted orthopaedic interventions.

Acknowledgements

References

1. Stiehl JB, Konermann WH, Haaker RG, DiGioia AM III. *Navigation and MIS in Orthopaedic Surgery*. Springer-Verlag: Berlin, 2007.
2. Bainville E, Bricault I, Cinquin P, Lavallée S. Concepts and methods of registration for computer-integrated surgery. In *Computer-assisted Orthopedic Surgery*. Hogrefe & Huber: Bern, Switzerland, 1999; 15–34.
3. Laine T, Lund T, Ylikoski M, *et al*. Accuracy of pedicle screw insertion with and without computer assistance: a randomised controlled clinical study in 100 consecutive patients. *EuroSpine J* 2000; **9**: 35–40.
4. Amin DV, Kanade T, DiGioia AM III, *et al*. Ultrasound-based registration of the pelvic bone surface for surgical navigation. In Abstracts from CAOS International 2001–1st Annual Meeting of the International Society for Computer-assisted Orthopaedic Surgery, Davos, Switzerland, 7–10 February 2001; *Comput Aid Surg* 2001; **6**: 48.
5. Amstutz C, Kowal J, Sati M, Nolte L-P. A-mode ultrasound as a tool for non-invasive registration. In Proceedings of the 5th International Symposium on Computer-assisted Orthopaedic Surgery, 17–19 February 2000; Davos, Switzerland; 49.
6. Barratt DC, Penney GP, Chan CS, *et al*. Self-calibrating 3D-ultrasound-based bone registration for minimally invasive orthopaedic surgery. *IEEE Trans Med Imag* 2006; **25**(3): 312–323.
7. Ionescu G, Lavallée S, Demongeot J. Automated registration of ultrasound with CT images: application to computer-assisted prostate radiotherapy and orthopedics. In *Medical Image Computing and Computer-assisted Intervention (MICCAI)*. Springer-Verlag: Berlin, 1999; 768–777.
8. Maurer CR Jr, Gaston RP, Hill DLG, *et al*. AcouStick: a tracked A-mode ultrasonography system for registration in image-guided surgery. In *Medical Image Computing and Computer-assisted Intervention (MICCAI)*. Springer-Verlag: Berlin, 1999; 953–962.
9. Tonetti J, Carrat L, Lavallée S, *et al*. Ultrasound-based registration for percutaneous computer-assisted pelvis surgery: application to iliosacral screwing of pelvis ring fractures. In *Computer-assisted Radiology and Surgery*. Elsevier Science: Amsterdam, 1997; 961–966.
10. Thomas JG, Peters RA III, Jeanty P. Automatic segmentation of ultrasound images using morphological operators. *IEEE Trans Med Imag* 1991; **10**(2): 180–186.
11. Roche A, Pennec X, Malandain G, Ayache N. Rigid registration of 3D ultrasound with MR images: a new approach combining intensity and gradient information. *IEEE Trans Med Imag* 2001; **20**(10): 1038–1049.
12. Daanen V, Tonetti J, Troccaz J. A fully automated method for the delineation of osseous interface in ultrasound images. In *Medical Image Computing and Computer-assisted Intervention (MICCAI)*. Springer-Verlag: Berlin, 2004; 549–557.

13. Jain AK, Taylor RH. Understanding bone responses in B-mode ultrasound images and automatic bone surface extraction using a Bayesian probabilistic framework. In *Medical Imaging 2004: Ultrasonic Imaging and Signal Processing*, Walker WF, Emelianov SY (eds); *Proc SPIE* 2004; **5373** 131–142.

14. Yu Y, Acton ST. Edge detection in ultrasound imagery using the instantaneous coefficient of variation. *IEEE Trans Imag Proc* 2004; **13**(12): 1640–1655.

15. Moghari M, Abolmaesumi P. A novel incremental technique for ultrasound to ct bone surface registration using unscented Kalman filter. In *Medical Image Computing and Computer-assisted Intervention (MICCAI)*. Springer-Verlag: Berlin, 2005; 197–204.

16. Bächler R, Bunke H, Nolte L-P. Restricted surface matching – numerical optimization and technical evaluation. *Comput Aid Surg* 2001; **6**(3): 143–152.

17. Castelman KR. *Digital Image Processing*. Prentice Hall: New York, NJ, 1995.

18. Soille P. *Morphological Image Analysis*. Springer-Verlag: Berlin, 1999.

19. Rosenfeld A, Pfaltz JL. Sequential operations in digital picture processing. *J Am Coll Med* 1966; **13**(4): 471–494.

20. MARVIN object oriented application framework for medical applications; MEM Research Centre for Orthopaedic Surgery: https://choroidea.unibe.ch/marvin.

21. Kowal J, Amstutz CA, Nolte L-P. Comparison of three difference ultrasound B-mode calibration methods. In Proceedings of the 2nd Annual Meeting of the International Society for Computer-assisted Orthopaedic Surgery, 19–22 June 2002, Santa Fe, New Mexico, 2002; 293–294.

22. Bächler R Oberflächen basierte Registrierung für orthopädische und HNO Anwendungen. PhD Thesis, M. E. Mueller Institute for Biomechanics, University of Bern, Switzerland, 2000.

23. Glatard T, Montagnat J, Pennec X. Medical image registration algorithms assesment: bronze standard application enactment on grids using the moteur workflow engine. *Stud Health Technol Inform* 2006; **120**: 93–103.

24. Hüsler J, Zimmermann H. *Statistische Prinzipien für medizinische Projekte*. Verlag Hans Huber: Bern, Switzerland, 1996.